ADVANCED ENERGY & SUSTAINABILITY RESEARCH Open Access

www.advenergysustres.com

Tailoring the Electron-Deficient Central Core on Fused-Ring Nonfullerene Acceptors: Deciphering the Relationships Between Structure, Property, and Photovoltaic Performance

Fátima Suárez-Blas, Lorenzo Pandolfi, Matías J. Alonso-Navarro, Sergi Riera-Galindo, José Ignacio Martínez, Bernhard Dörling, Alejandro Funes, Albert Harillo-Baños, Elisabetta Venuti, María Mar Ramos, Mariano Campoy-Quiles, and José L. Segura**

In the field of organic solar cells, organic semiconductors with Y6-based chemical structure and their corresponding quinoxaline-based assemblies are settled down as promising materials in the field of OSCs. However, the chemical structure of Y6 derivatives does not allow an expansion in the electron-withdrawing central core, in contrast to their quinoxaline-based analogues. For this reason, herein, two different quinoxaline-based A–D–A′–D–A derivatives with 2D π-extended cores endowed with electroactive rylenimide moieties, named as Y6-1Napht and Y6-1Pery, are designed and synthesized. These enlarged fused-ring electron acceptors (FREAs) allow to study the influence of the length of the ryleneimide moiety on its structural, optical, electrochemical, and thermal properties as well as the tailoring of the frontier molecular orbitals. These results are also supported by quantum chemical calculations and photoluminescence measurements that provide additional information about their thermal stability and the microstructure of the films. Finally, as a proof of concept and to study the influence of these chemical modifications on the central core, solar cells based on these π-conjugated nonfullerene acceptors are fabricated.

1. Introduction

Within the family of nonfullerene acceptors (NFAs) reported so far, the first breakthrough was made in 2015 by Zhan et al.[1] who developed a novel nonfullerene fused-ring electron acceptor (FREA) with acceptor–donor–acceptor (A–D–A) structure. Since then, it has been observed that those systems endowed with FREAs show the best performances in photovoltaic devices. This is a consequence of a combination of wide absorption profiles, suitably aligned energy levels, high absorption coefficients, and good miscibility with complementary electron–donor polymers.[1,2]

To further improve the photovoltaic performances of FREAs, it has been shown that their electron affinity can be fine tuned by the introduction of an electron-withdrawing moiety (A′) in the middle of the central core of A–D–A molecules to create a charge-deficient region in A–DA′D–A structures.[3] Specially remarkable among these A–DA′D–A small-molecule acceptors is the Y6 system (**Figure 1**) that stands out for its contribution for the development of organic solar cells (OSCs).[4] Molecular engineering has been used to develop the so-called Y series of NFAs with high electron mobilities, low voltage loss, strong absorption in the near-infrared (NIR) region, and unique molecular configurations

---

F. Suárez-Blas, M. J. Alonso-Navarro, A. Funes, J. L. Segura
Department of Organic Chemistry
Faculty of Chemistry
Complutense University of Madrid
28040 Madrid, Spain
E-mail: segura@quim.ucm.es

F. Suárez-Blas, M. J. Alonso-Navarro, M. M. Ramos
Chemical and Environmental Technology Department
Rey Juan Carlos University
28933 Móstoles, Spain

The ORCID identification number(s) for the author(s) of this article can be found under https://doi.org/10.1002/aesr.202400028.

DOI: 10.1002/aesr.202400028

L. Pandolfi, S. Riera-Galindo, B. Dörling, A. Harillo-Baños, M. Campoy-Quiles
Institute of Materials Science of Barcelona
ICMAB-CSIC
08193 Bellaterra, Spain
E-mail: mcampoy@icmab.es

L. Pandolfi, E. Venuti
Dipartimento di Chimica Industriale "Toso Montanari"
Università di Bologna
Viale del Risorgimento, 4, 40136 Bologna, Italy

J. I. Martínez
Department of Low-dimensional Materials
Institute of Materials Science of Madrid (ICMM-CSIC)
28049 Madrid, Spain

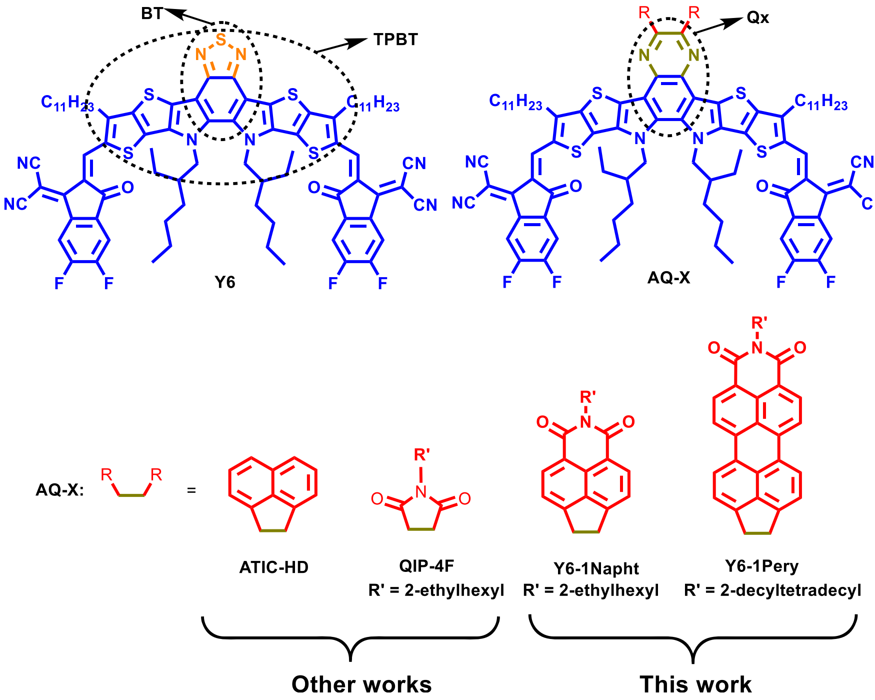

Figure 1. (Top left) Structure of the prototypical A–DA'D–A molecular system **Y6** with the dithienothiophen[3.2-b]-pyrrolobenzothiadiazole (**TPBT**) backbone and the benzothiadiazole (BT) moiety highlighted. (Top right) General molecular structure of Y6 analogues **AQ-X** where the benzothiadiazole- (BT-) fused core of Y6 derivatives is replaced by quinoxaline- (Qx-) fused cores. (Bottom) Structures of the AQ-X derivatives previously synthesized in other works **ATIC-HD**[11] and **QIP-4F**[13] and the novel systems studied in this article (**Y6-1Napht** and **Y6-1Pery**).

that have provided efficiencies above 18% in single-junction devices.[4d]

There are mainly three aspects that have been engineered to optimize the structure of Y series FREAs: 1) terminal engineering to adjust absorption, energy levels, charge dynamics, and blend morphology,[5] 2) alkyl chain engineering to bring the steric hindrance effect to get less energetic disorder and improve the solubility of materials,[6] and 3) core engineering through the development of new central building blocks that facilitate the generation of appropriate morphologies for the bulk heterojunction light-harvesting layer, regulate the energy levels, and expedite the charge-carrier transport.[7]

Concerning the last approach aimed in the development of new central building blocks, one of the most employed electron-poor units is 2,1,3-benzothiadiazole (**BT**). Because of its commercial availability and its *sp*^{2}-hybridized nitrogen atoms that endow **BT** with electron-withdrawing character, this heterocyclic moiety has become very popular in constructing low-bandgap conjugated materials.[8] Thus, the BT-core-based fused unit, dithienothiophen[3.2-b]-pyrrolobenzothiadiazole (**TPBT**, Figure 1), has been extensively used to synthesize FREAs of the Y series because it preserves the conjugation along the length of the molecule, thus allowing the tuning of the electron affinity.[4c]

Despite the unique characteristics of benzothiadiazole, this heterocyclic moiety does not allow a fused 2D expansion of the NFAs of the Y series to improve the packing arrangements.[9] In this respect, an alternative central building unit that allows the fused 2D expansion of the NFAs is the pyrazine moiety. The substitution of the **BT** moiety of the Y series by a pyrazine moiety leads to the formation of a quinoxaline.[10] When the quinoxaline system is fused with the thieno[3,4-b]thiophene moieties of the conjugated backbone, novel NFAs can be obtained (**AQX**, Figure 1) with appropriate frontier molecular orbital energy levels, exceptionally extended absorption cross section with high absorption coefficients and low reorganization energy that facilitate electron transport and intermolecular packing.[4c,7f] Further 2D expansion with acenaphthene by fusing it with the quinoxaline system in NFAs (**ATIC-HD**, Figure 1) has proven to be also an effective strategy to adjust the aggregation behavior to design high-crystallinity materials.[11] On the other hand, fusion of quinoxaline with imide units is an efficient strategy to synthesize electron acceptor building blocks to be incorporated in donor–acceptor-type small molecules and conjugated polymers for organic electronic devices.[12] Thus, Ying et al.[13] fused electron-withdrawing quinoxalineimide units with two thieno[3,2-b′]thiophene moieties through a nitrogen atom as the bridge to lead a *π*-conjugated planar NFA (**QIP-4F**, Figure 1) with high performance in OSCs.

In this work, we have designed and synthesized a family of nonfullerene FREA systems with A–DA′D–A structures in which the A′ central building blocks consist of quinoxaline units fused with ryleneimide moieties (namely, **Y6-1Napht** and **Y6-1Pery**, Figure 1). Rylene diimide derivatives have been chosen for the fused 2D expansion of NFAs because of their excellent electrochemical and optical properties, their high photochemical and thermal stability, their robustness, as well as their tunable molecular orbital energy levels and topologies.[14] The formation of the new assemblies is confirmed by spectroscopic techniques and a combined study of their solution and solid-state absorption, together with the characterization of their electrochemical properties, is presented. We have additionally made a first evaluation of the potential of this type of molecule as NFAs in OSCs.

2. Results and Discussion

The detailed synthetic route to **Y6-1Napht** and **Y6-1Pery** is shown in **Scheme 1**, and all the new compounds have been characterized in depth by suitable spectroscopic and analytical methods (see Supporting Information). Quinoxaline derivatives are usually obtained by condensation reactions between diamines and diketones.[15] Thus, for the synthesis of the target compounds, we used as starting material the dithienothiophen[3,2-b]-pyrrolobenzothiadiazole (**1**),[16] which was subsequently reduced with nonactivated zinc dust in acetic acid at 140 °C for 30 min to yield the diamino derivative **2**, which was in situ reacted with the corresponding functionalized 1,2-diketone ryleneimides **3** or **4**. Naphthalimide[17] and peryleneimide-based[18] 1,2-diketones were first described by Segura and co-workers and successfully used as versatile electron-withdrawing building blocks for the synthesis of small molecules,[17] macromolecular,[19] linear,[20] 2D,[21] 3D,[22] and amphiphilic[23] organic semiconductors with applications in organic field effect transistors (OFETs),[24] organic solar cells (OSCs),[25] and as photo-[26] and photoelectrocatalysts.[27]

The remaining synthesis steps for the target compounds are commonly used in the synthesis of NFAs and involve first the formylation of **5** and **6** via the Vilsmeier–Haack reaction to yield the corresponding dialdehydes **7** and **8**. The subsequent Knoevenagel condensation of **7** and **8** with 2-(5,6-difluoro-3-oxo-2,3-dihydro-1 H-inden-1-ylidene)malononitrile (**9**) afforded the target fused 2D expanded NFAs **Y6-1Napht** and **Y6-1Pery** as blue and purple solids, respectively (Scheme 1).

Despite the large rigidity and planarity of the backbones imparted by the large number of fused rings present in **Y6-1Napht** (12 fused rings) and **Y6-1Pery** (15 fused rings), the attached linear and branched alkyl chains provide them good solubilities in common chlorinated solvents. For instance, in chloroform, **Y6-1Napht** and **Y6-1Pery** show solubility values of 19.8 and 15.2 mg mL^{-1}, respectively. Thus, proper spectroscopic and spectrometric characterization can be carried out not only by Fourier transform-infrared (FT-IR) and high-resolution mass spectrometry (matrix-assisted laser desorption/ionization) but also by nuclear magnetic resonance (NMR) in solution. In addition, **Y6** semiconductor, first described by Yuan et al.[4c] was also synthesized for comparison purposes.

The analysis of the ^{1}H-NMR spectra (Figure S3 and S6, Supporting Information) in deuterated chloroform shows the

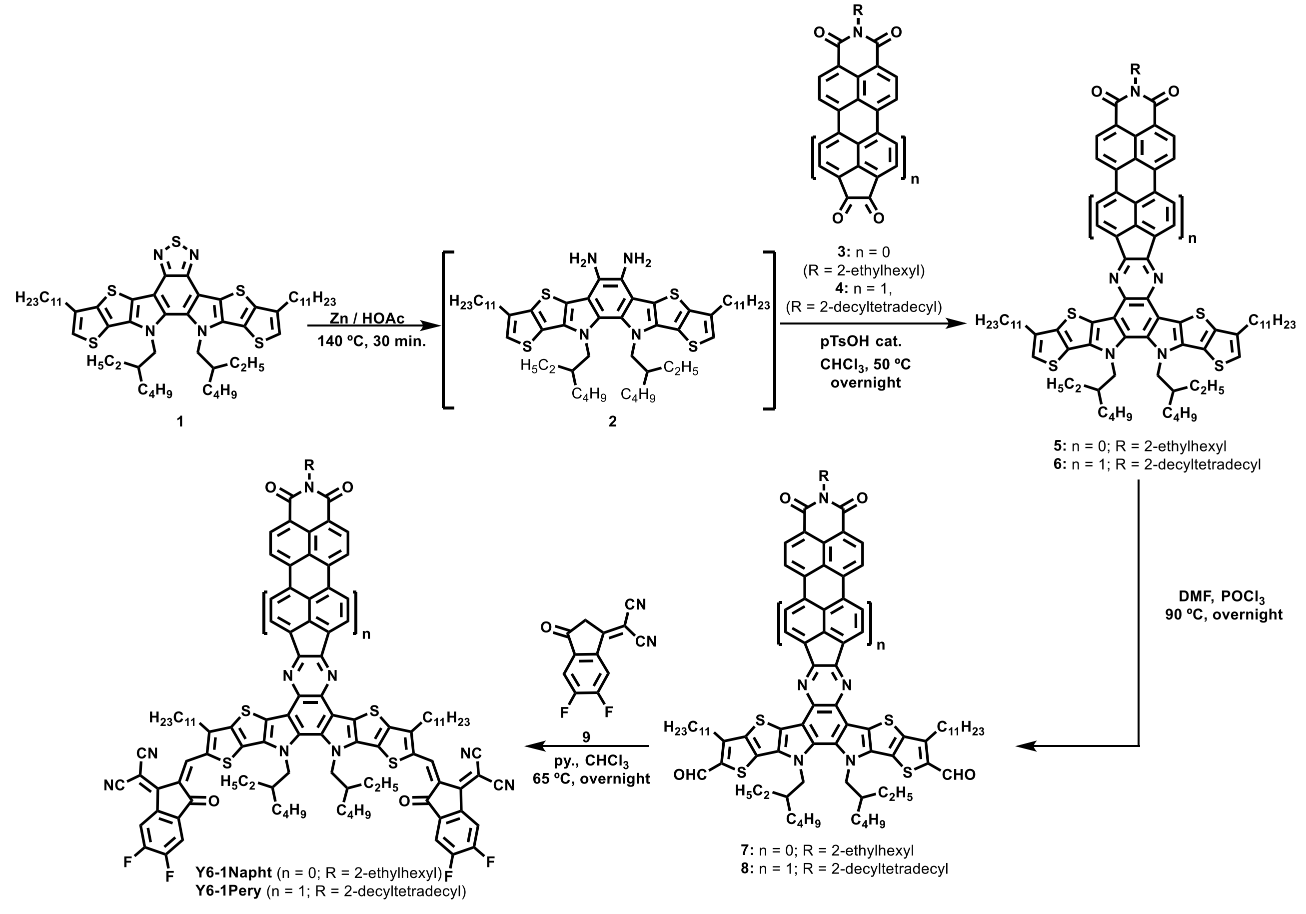

Scheme 1. Synthetic route for **Y6-1Napht** and **Y6-1Pery**.

presence of the characteristic signals corresponding to the hydrogen atoms of the naphthalene-1,8-dicarboximide and perylene-3,4-dicarboximide moieties in **Y6-1Napht** and **Y6-1Pery** assemblies. First, both present the most deshielded singlet ascribed to the hydrogen atoms of the vinylene group around 9.00 ppm for **Y6-1Napht** and at 8.60 ppm for **Y6-1Pery**. Then, the signals corresponding to the naphthalimide and perylenimide units appear between 8.70 and 8.40 for **Y6-1Napht** as well-defined doublets and between 8.50 and 7.90 ppm for **Y6-1Pery** as broad singlets. Finally, the corresponding hydrogen atoms of the fluorinated end-capped electron-acceptor units appear as two multiplet signals at 8.45 and 7.60 ppm in both semiconductors. In addition to this, all these NFAs present the corresponding signals for the alkyl chains at higher field, highlighting the doublets of the methylenes directly connected to the nitrogen atom of the imide group at 4.20 ppm in **Y6-1Napht** and **Y6-1Pery**.

Regarding the ^{13}C-NMR spectra, **Y6-1Napht** possesses the signal of the carbonyl unit of the end-capped electron-acceptor unit at 184 ppm, followed by the signal of the imide group at 165 ppm. Then, a myriad of C_{sp}^{2} signals appear between 155 and 110 ppm, pointing out the one ascribed to the pyrazine unit at 156 ppm (Figure S9, Supporting Information). With respect to the **Y6-1Pery** derivative, despite the good solubility it presents in deuterated chloroform, its π-extended T-shape skeleton with 15 fused-ring units does not allow obtaining a well-resolved ^{13}C-NMR spectrum.

In the IR spectra of all these perylenimide-based NFAs (Figure S13 and S16, Supporting Information), it is possible to observe the diagnostic stretching bands corresponding to the imide groups of **Y6-1Napht** and **Y6-1Pery** around 1700 cm^{-1}, followed by the stretching band ascribed to the pyrazine ring at 1640 cm^{-1}. Finally, an intense and characteristic C≡N tension is also observed around 2300 cm^{-1} corresponding to the fluorinated end-capped electron-acceptor units. Finally, additional evidence regarding the structures proposed for these novel assemblies can be obtained by mass spectrometry analyses, which provided mass values, which are in good agreement with the expected ones for **Y6-1Napht** and **Y6-1Pery** π-conjugated semiconductors (Figure S19 and S22, Supporting Information).

We complemented the vibrational study by measuring and simulating the corresponding Raman spectra for the two systems and the Y6 reference. The most intense peaks measured experimentally are shown in **Figure 2** for **Y6-1Napht**, **Y6-1Pery**, and **Y6**. Some peaks are common to all compounds, relating to the parent Y6 core, such as the intense aromatic C=C stretching of the central rings, which is found at 1555 cm^{-1} for Y6, at 1560 cm^{-1} for **Y6-1Napht**, and at 1588 for **Y6-1Pery**, or the stretching mode which involves the C and N atoms of the Y6 core at around 1506 cm^{-1} for **Y6** and at 1515 cm^{-1} for **Y6-1Napht**. However, some distinctive peaks aid the identification of the derivative functional group, the mode at 1628 cm^{-1}, corresponding to the motion of the "Pery" substituent group, displayed only by the **Y6-1Pery** compound. Density functional theory (DFT) simulated the Raman spectra and helped to confirm the peak assignment. The B3LYP functional in combination with the 3-21G* basis set was applied for the calculations, and the output wavenumbers were shifted by a factor of 0.961, while the calculated intensities were corrected by the temperature factor ($T = 298$ K) and the excitation wavelength factors ($\lambda_{ex} = 488$ nm).[28] To allow the system energy convergence, the compounds were simulated by removing the lateral C8 alkyl chains, which were replaced by a hydrogen atom. The simulated patterns shown in Figure S23, Supporting Information, reproduce the isolated molecule spectra of the Y6 derivatives in the energy interval detected by Raman spectroscopy (200–2300 cm^{-1}). In the close-up of Figure S23, Supporting Information, the comparison between the DFT-simulated spectra and the data from the measurements of the **Y6**, **Y6-1Napht**, and **Y6-1Pery** thin films is shown, where the most intense and characteristic peaks can be assigned (Table S1, Supporting Information). It should be noted that the vibrational analysis is carried out based on the simulations performed on the isolated molecule. This approximation is not completely accurate because interactions between not translationally equivalent molecules in the crystal unit cell generally result in the splitting of each intramolecular vibration into a number of terms equal to the number Z of molecules/cell. However, such splits, and the associated energy shifts, are usually negligible and anyway detectable, when symmetry selection rules apply, in Raman measurements in polarized light.[29]

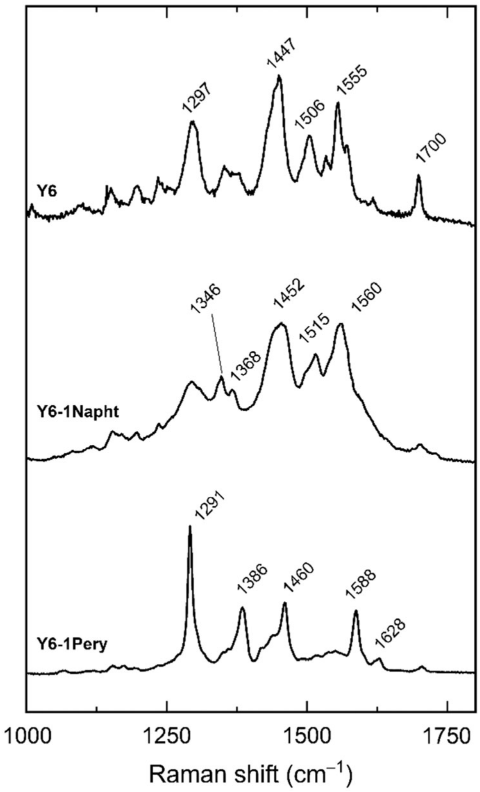

Figure 2. Experimental Raman spectra of **Y6**, **Y6-1Napht,** and **Y6-1Pery** intramolecular modes in the fingerprint region (1000–1750 cm^{-1}).

UV–vis absorption and emission measurements as well as cyclic voltammetry (CV) analyses have been carried out to evaluate the optical and electrochemical properties of these novel NFAs. **Table 1** and **2** summarize the most relevant values obtained from these techniques.

Table 1. Physicochemical properties obtained from the UV–vis absorption measurements in chloroform solutions and thin films for **Y6**, **Y6-1Napht,** and **Y6-1Pery**.

	[C] [10^{-6} mol L^{-1}]	$\lambda_{abs}^{max, sol}$ [nm]	$\varepsilon_{\lambda}^{max, sol}$ [L mol^{-1} cm^{-1}]	λ_{abs}^{onset}[nm]	$\lambda_{abs}^{max, film}$ [nm]	λ_{film}^{onset} [nm]	$\lambda_{em}^{max, sol}$ [nm]	E_g^{opt} [eV]
Y6	1.0	731	3.08×10^5	789	850	919	793	1.57
Y6-1Napht	1.0	730	2.70×10^5	782	784	869	769	1.59
Y6-1Pery	1.0	743	3.41×10^5	805	809	890	789	1.54

The energy bandgap is derived from the low-energy absorption edge using the equation $E_g^{opt} = 1240/\lambda^{onset}$.

Table 2. Electrochemical data.

	$E_{redI}$$^{a)}$ [V]	$E_{oxI}$$^{a)}$ [V]	LUMO$^{b)}$ [eV]	HOMO$^{c)}$ [eV]	$E_g^{elec.,d)}$ [eV]
Y6	−0.82	+0.60	−4.28	−5.70	1.42
Y6-1Napht	−0.92	+0.57	−4.18	−5.67	1.49
Y6-1Pery	−0.92	+0.51	−4.18	−5.61	1.43

$^{a)}$Electrochemical data obtained from CV experiments carried out in DCM/TBAPF$_6$ (0.1 M) solutions at a scan rate of 0.1 V s^{-1}, using Pt as working and the counter electrodes, and the Fc/Fc$^+$ redox couple as internal reference. $^{b)}$Estimated from $E_{LUMO} = -5.1$ eV $- E_{redI}$. $^{c)}$Estimated from $E_{LUMO} = -5.1$ eV $- E_{oxI}$. $^{d)}$Estimated from $E_g^{elec.} = E_{HOMO} - E_{LUMO}$.

As shown in **Figure 3**a, in the range of 500–800 nm, the UV–vis–NIR absorption spectra of both **Y6-1Napht** and **Y6-1Pery** assemblies present similar absorption profiles to that observed for the **Y6** derivative, which are related to their strong intramolecular charge transfer (ICT) characteristics.[4] The maximum molar absorption coefficients in chloroform solutions are 3.08×10^5, 2.70×10^5, and 3.41×10^5 L mol^{-1} cm^{-1}, related to the maximum wavelengths at 731, 730, and 743 nm for **Y6**, **Y6-1Napht**, and **Y6-1Pery**, respectively. It is worth mentioning that, in comparison with the previous quinoxaline-based analogues described in the literature, **Y6-1Napht** and **Y6-1Pery** are, to the best of our knowledge, the first molecular assemblies that display no difference or a redshift in the $\lambda_{abs}{}^{max}$ in solution when a pyrazine moiety replaces the typical benzothiadiazole core in the same structure described for **Y6**.[4c] With the aim to study the effect of vertical π-conjugated extension in these NFAs, the naphthalimide unit was replaced by its larger analogue, the perylenimide, in **Y6-1Pery**. This new molecular assembly shows a more intense and redshifted (12 nm vs. **Y6**) ICT absorption band in solution. The optical bandgaps of **Y6-1Napht** and **Y6-1Pery** are 1.59 and 1.54 eV, both estimated from their absorption onsets at 782 and 805 nm, respectively.

Due to the extended π-conjugated backbones present in both **Y6-1Napht** and **Y6-1Pery** molecular semiconductors, concentration-dependent experiments were carried out to study the feasible formation of supramolecular aggregates in solution. Interestingly, despite the larger structure with several fused rings, as compared to the **Y6** analogue, there is no significant evidence of self-assembled structures in chloroform solutions similarly to that observed for **Y6** (Figure S25, S29, Supporting Information). The lack of self-assembled nanostructures of **Y6** in solution is known to occur mainly due to two reasons: 1) first, the presence of long and branched alkyl chains which promotes steric hindrance between molecules, destabilizing the formation of aggregates in solution,[13,30] and 2) the preferential interactions between the end-capped moieties instead of the π–π interactions between the π-conjugated backbone with several fused rings.[11,31] To address the aggregation tendencies of **Y6-1Napht** and **Y6-1Pery**, in comparison with that of **Y6**, we have carried out a large battery of DFT-based theoretical calculations by the Gaussian16 simulation package,[32] within the B3LYP/6-311G** level of theory,[33] of the different molecular systems. From the result of these calculations, we can extract some valuable information. In a first step, we computed the most stable conformation of **Y6-1Napht** and **Y6-1Pery** (see **Figure 4**). These calculations were performed using both the full length of the alkyl chains or, in a reduced model, by just considering only methyl substituents as models instead of the long alkyl chains. This strategy led to identical optimized structures for the π-conjugated backbone independently of the size of the alkyl chains adopted in the calculations.

After this initial step, and with the main goal to study the preferential coupling between molecules, a dimeric scenario is proposed with different possible interaction configurations between molecules (**Figure 5**). The molecular packing sketch map for **Y6** has been previously reported using single crystal X-Ray diffraction, showing that the **Y6** molecules overlay on top of another two **Y6** molecules through the end groups stacking.[34] The result of similar theoretical calculations for the **Y6-1Napht** and **Y6-1Pery** dimers reveals that, apart from the end groups stacking, the presence of naphthalimide–naphthalimide and perylenimide–perylenimide interactions (Figure 5) cannot be ruled out. Considering that the arrangement of the end groups observed for **Y6** provides the formation of transporting channels to facilitate the carrier transport, the presence of alternative interactions in **Y6-1Napht** and **Y6-1Pery** seems to be detrimental for the achievement of suitable transporting channels[35] in blends with polymer donors for organic photovoltaics (OPV), as shown below. The different stacking modes are probably responsible also for the different solubility values, which drop slightly when the π-conjugated structure is expanded. This decrease in solubility has been also observed in Y6 derivatives endowed with π-extended phenanthrene systems,[11] where the introduction of these units leads to stronger π–π interactions. Furthermore, this decrease in solubility is further accentuated by the presence of rigid and flat pyrazine connectors.[36]

In addition, the optical properties of these new materials were also studied in solid state, and the results are depicted in Figure 3b. The broader and redshifted absorption profiles for

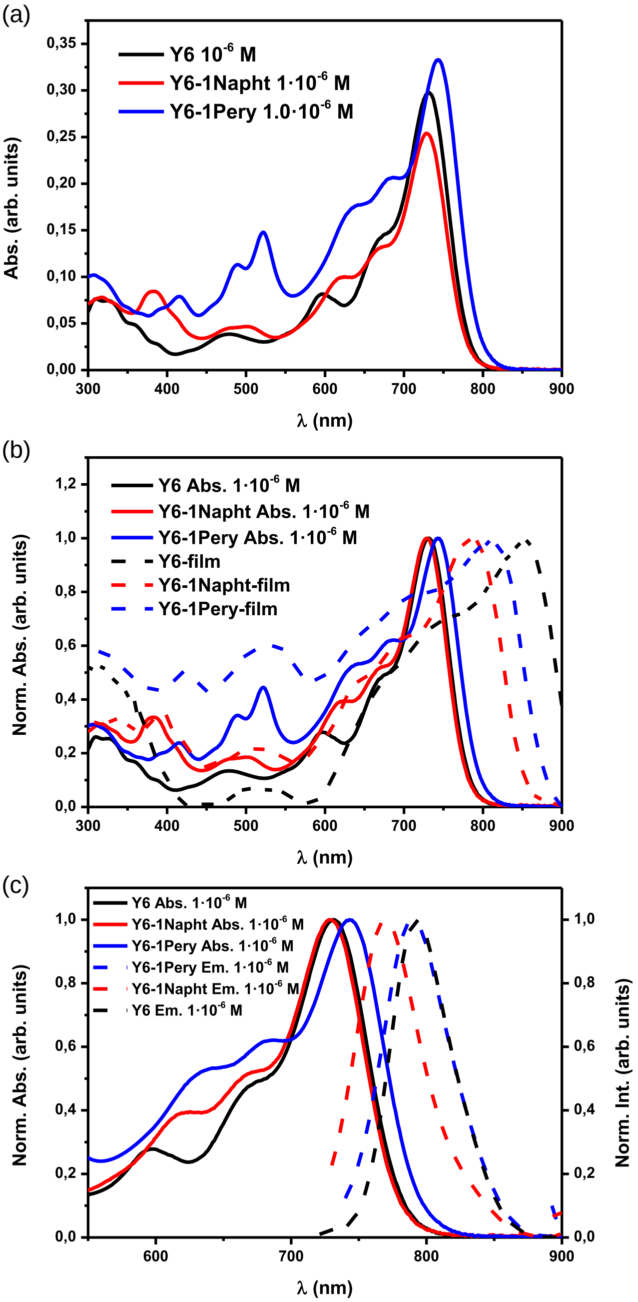

Figure 3. a) UV–vis absorption profiles in chloroform solutions. b) A comparison between chloroform solution (solid) and thin-film (dashed) absorption spectra. c) Normalized absorption (solid) and emission (dashed) spectra in chloroform solution for **Y6** (black), **Y6-1Napht** (red), and **Y6-1Pery** (blue).

Y6-1Napht and **Y6-1Pery** in thin films in comparison with **Y6** are probably due to the aforementioned intermolecular interaction between the naphthalimide or perylenimide units, which are present, respectively, in **Y6-1Napht** and **Y6-1Pery**. Also noteworthy is the smaller Stokes shift observed for **Y6-1Napht** and **Y6-1Pery** in comparison with that observed for **Y6** (Figure 3c). These reduced Stokes shift values are indicative of a lower relaxation of their corresponding excited states, which is beneficial for the voltage losses associated with the photovoltaic process.[31] This fact is also consistent with the calculated reorganization energies. Indeed, the smaller reorganization energies have been determined for **Y6-1Napht** and **Y6-1Pery** in comparison with **Y6**, in which λ_e values (radical anion, eV) are 0.15, 0.14, and 0.11 and λ_h values (radical cation, eV) are 0.19, 0.18, and 0.16 for **Y6**, **Y6-1Napht**, and **Y6-1Pery**, respectively.

The UV–vis absorption pattern is accurately reproduced by time dependent-density functional theory (TD-DFT) calculations (Table S2, Supporting Information), where the most redshifted absorption bands for Y6-1Napht and Y6-1Pery are ascribed to a one-electron excitation, from the highest occupied molecular orbital (HOMO) to the lowest unoccupied molecular orbital (LUMO), being both frontier molecular orbitals delocalized over the entire π-conjugated backbone. In the case of **Y6-1Napht** and **Y6-1Pery**, the HOMOs are delocalized also over the perylenimide fragment, as depicted in **Figure 6**b. Thus, the introduction of perylenimide and pyrazine fragments in replacement of the thiadiazole unit (**Y6-1Napht** and **Y6-1Pery** vs. **Y6**) can be used as an efficient tool to precisely tune the topology of the HOMO energy level without modifying the topology of the LUMO energy level.

CV analyses in solution were performed to evaluate the electrochemical properties of these new π-extended assemblies and to estimate the frontier orbital energy levels. The as-obtained results are shown in Figure 6a, S32, and S33, Supporting Information and summarized in Table 2.

The LUMO and HOMO energy levels for these π-extended perylenimide-based NFAs **Y6-1Napht** and **Y6-1Pery** can be estimated from the onsets of the first reduction potential and the first oxidation potential processes obtained by CV measurements in solution (Table 2). CV measurements of **Y6** have been also performed for comparison purposes. As shown in Figure 6a, the three compounds exhibit an ambipolar behavior with both oxidation and reduction processes. The reduction processes for **Y6-1Napht** and **Y6-1Pery** are irreversible, similarly to that previously reported for **Y6**. On the other hand, the introduction of a pyrazine unit instead of the thiadiazole core leads to a slight destabilization of the LUMO values, because of the weaker electron-acceptor ability of the pyrazine moiety in comparison with the thiadiazole core.[37] The weaker electron-acceptor ability of the quinoxaline core in both **Y6-1Napht** and **Y6-1Pery** leads to higher lying LUMO energy levels, which is beneficial for obtaining higher V_{oc} values and decreasing the voltage loss of the exciton dissociation in OSCs, because of the smaller energy gap between the LUMO levels of the donor polymer **PM6** and the electron acceptors.[38]

On the other hand, the oxidation processes shown in the CV experiments are likely reversible in all the semiconductors, but the introduction of different π-extended units in the central core leads to a destabilization in the HOMO energy level of **Y6-1Pery** compared to that of **Y6-1Napht**, in accordance with the larger π-extended system of the perylene derivative. Thus, these synthetic modifications allow modulating the HOMO energy values, which is a key parameter to achieve a more efficient exciton generation between the small-molecule NFA and the donor polymer and thus obtain small energy losses (E_{loss}).[30,39] It is also interesting to note the good concordance observed between the electrochemical bandgap ($E_{\text{gap}}{}^{\text{elec}}$) values and the optical bandgap

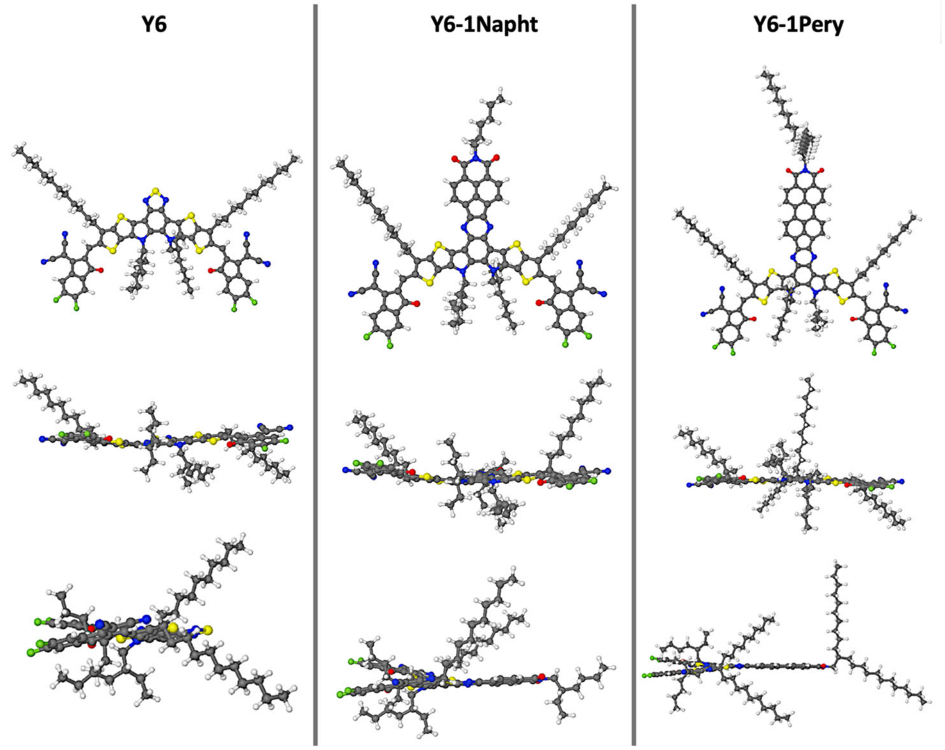

Figure 4. Top and two side views of the DFT-computed optimized geometry for **Y6** (left), **Y6-1Napht** (center), and **Y6-1Pery** (right) at the B3LYP/6-31G** level of theory.

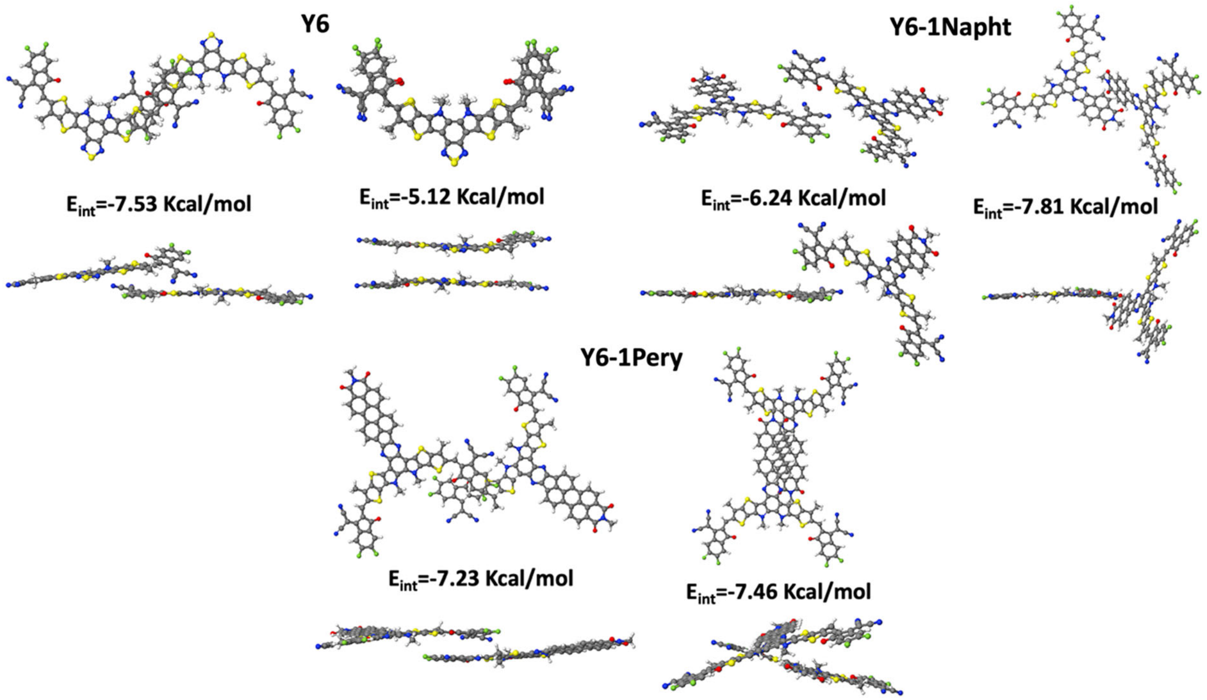

Figure 5. Top and side views of the DFT-computed optimized geometry for the most stable **Y6**, **Y6-1Napht,** and **Y6-1Pery** dimer configurations at the B3LYP/6-31G** level of theory. Calculated interaction energies of dimers are shown in each case in kcal mol^{-1}.

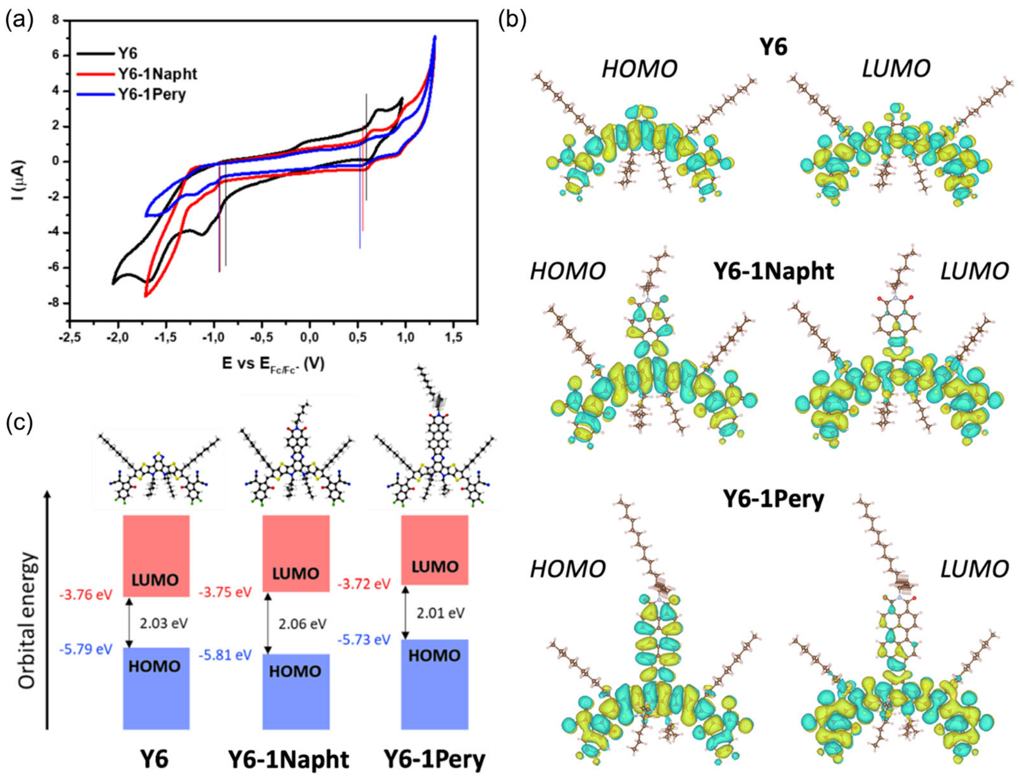

Figure 6. a) CV measurements for **Y6** (black), **Y6-1Napht** (red), and **Y6-1Pery** (blue) in dichloromethane solutions with 0.1 M of TBAHFP as supporting electrolyte. b) B3LYP/6-31G** molecular orbital topologies of Y6 (top), Y6-1Napht (center), and **Y6-1Pery** (bottom). c) Theoretical energy-level diagram for the SM-NFA **Y6-1Napht** (center) and **Y6-1Pery** (right) described in this work and the **Y6** reference acceptor (left).

(E_{gap}^{opt}) obtained from the onset of the most redshifted absorption.

Thermogravimetric analyses and differential scanning calorimetry measurements have been carried out (Figure S34–S37, Supporting Information) under nitrogen atmosphere to gain more information about the thermal stability of these molecular assemblies. These experiments showed no reliable evidence of phase transition processes in the selected range (30–300 °C) by DSC. In addition, TGA analyses only showed decomposition at temperatures above 200 °C for both **Y6-1Napht** and **Y6-1Pery**, which make them compatible with the requirements for the fabrication of devices.

To gain further insights into the thermal properties of the compounds in thin-film geometry, we used photoluminescence (PL).[40] Rather than monitoring the PL as a function of temperature, we used a recently demonstrated method in which the PL is collected at room temperature for a sample annealed at different temperatures.[41] Specifically, PL spectra of the **Y6**, **Y6-1Napht**, and **Y6-1Pery** thin films were collected as a function of the annealing temperature in an initially homogeneous film that was subjected to a gradient in thermal annealing. In **Figure 7**a, the series of PL spectra is shown for each compound, depending on the annealing temperature of the thin-film sample, from 70 to 250 °C (rainbow color palette, from violet to red). In Figure 7b, the PL maps of the same samples are shown to highlight the temperature dependence, with the variations in the intensities and the λ_{max} positions easier to visualize. In the case of **Y6** thin film, the broadband at around 920 nm (the 0–0 transition according to Wei et al.[42]) clearly increases in intensity with the substrate annealing temperature, reaching a maximum at 150 °C, and then decreases considerably while blueshifting and splitting into two components. The spectra of **Y6-1Napht** show a similar behavior: λ_{max} initially around 850 nm undergoes an abrupt blueshift, and a shoulder gains intensity when the annealing temperature reaches 125 °C, while gradually the overall intensity of the spectrum decreases. Finally, the spectra of **Y6-1Pery** ($\lambda_{max} \approx 875$ nm) displayed a gradual redshift at around 175 °C, but with changes in intensities similar to the other compounds. Thus, general trends can be highlighted as in the following: 1) substitution of the pristine **Y6** compound with the selected groups moved the emission maximum, depending on the number and the chemical nature of the substituent, which clearly influences the energy levels of the chromophore; 2) the Y6-derivatives with the "Napht" group showed a blueshift (hypochromic shift) with thermal annealing, while the "Pery" substitution displayed a redshift (bathochromic shift); and 3) the maximum emission intensity occurs at around 125 °C of annealing temperature for each Y6 derivative. Typically, the formation of solid-state H aggregates is accompanied by a blueshift with respect to the monomer absorption energy, while the emission quantum yield is reduced or null. In J-aggregates instead, a distinct redshift of the absorption takes place, coupled with an increase in the efficiency of fluorescence compared to the monomer.[43] Most likely, the thermal annealing, at least partially, led the system toward conditions of

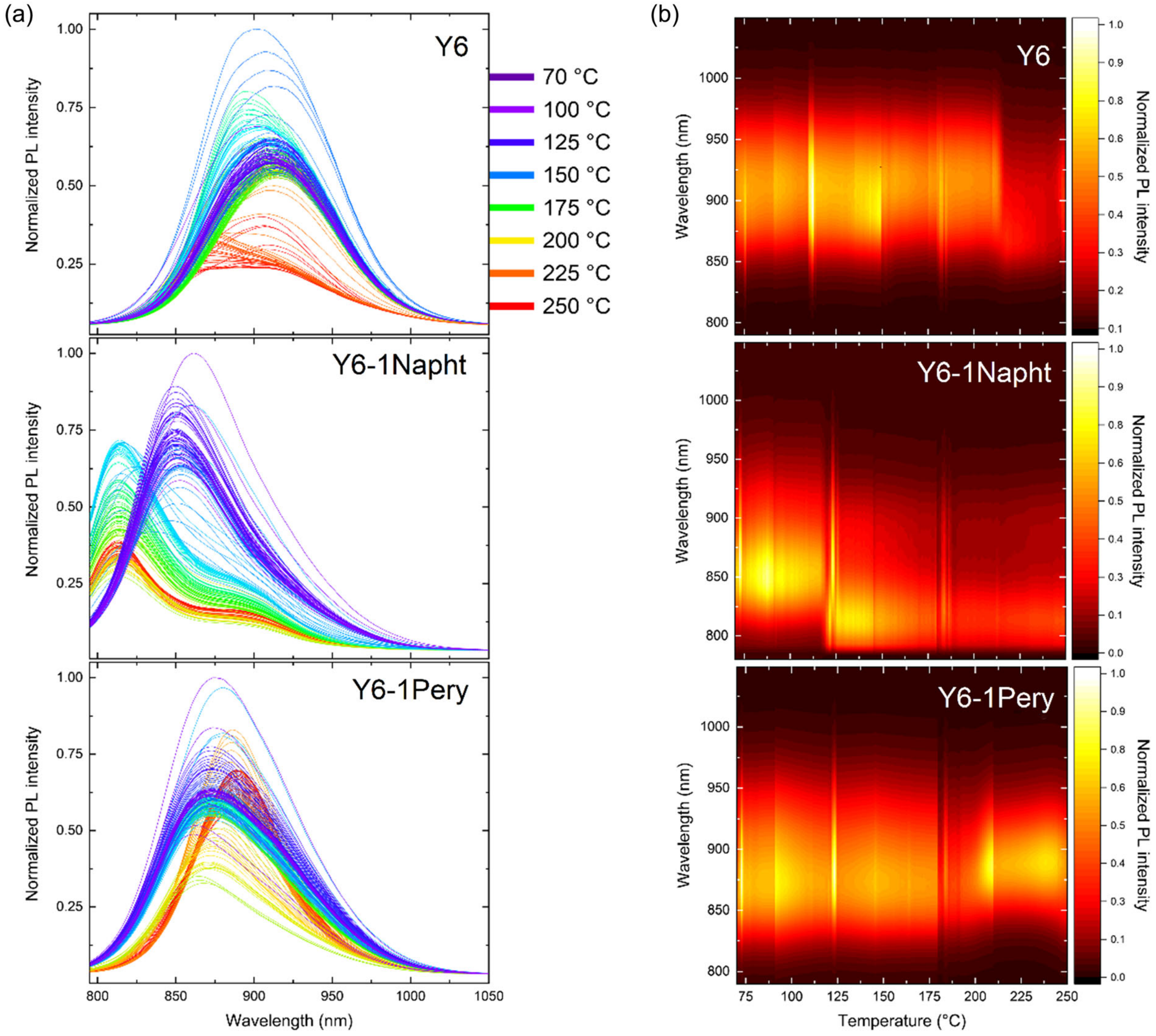

Figure 7. a) PL emission spectra and b) emission maps of the **Y6** and **Y6 derivatives** thin-film samples ($\lambda_{\text{exc}} = 785$ nm). The plots depend on the annealing temperature of the thin-film sample. Variations in intensity and peak position can be appreciated as a function of the annealing temperature.

thermodynamic equilibrium, enhancing the crystallization of the deposited less-ordered films. This would result in the reorganization of the molecules into crystal lattices in which either H-aggregates or J-aggregates are present. The former condition, that is, H-aggregation, would apply to the cases of "Napht" substitution, as suggested by the decreasing intensity after the maximum at 125 °C. For the case of "Pery" substitution, the presence of a second maximum around 200 °C after the maximum at 125 °C points to J-aggregation.

Martin et al.[44] suggested a rich polymorphism of **Y6** in a thin film for the temperature range of 180–230 °C. It is noteworthy that this corresponds to the annealing temperatures able to induce the most relevant changes in the PL spectra of our **Y6** thin-film samples. This finding could be explained by assuming that at a specific, higher temperature, the thermal annealing process in fact promotes the formation of a different crystal structure (Figure S38, Supporting Information), having also distinct PL properties. If this phase formation was genuine, the same concept could be extended to all the investigated molecules, identifying different temperature ranges for the existence of different solid phases. For **Y6-1Napht**, the abrupt emission blueshift occurs for the annealing temperature of 120 °C, lower than the one recorded for the parent molecule. Finally, a quickly appearing redshift is detected in **Y6-1Pery** around 190 °C.

The annealed thin-film samples were also studied by means of variable-angle spectroscopic ellipsometry (VASE). The results are shown in **Figure 8**, which displays the real (n) and imaginary (k) components of the refractive index, as determined by the ellipsometric measurements of the various compounds. The first observation is that the extinction coefficient is high for the three acceptors, in agreement with the measurements in solution, and also in agreement with published data for many high-performing NFAs.[45] Slightly lower maximum values are observed for **Y6-1Napht**, also in agreement with solution data.

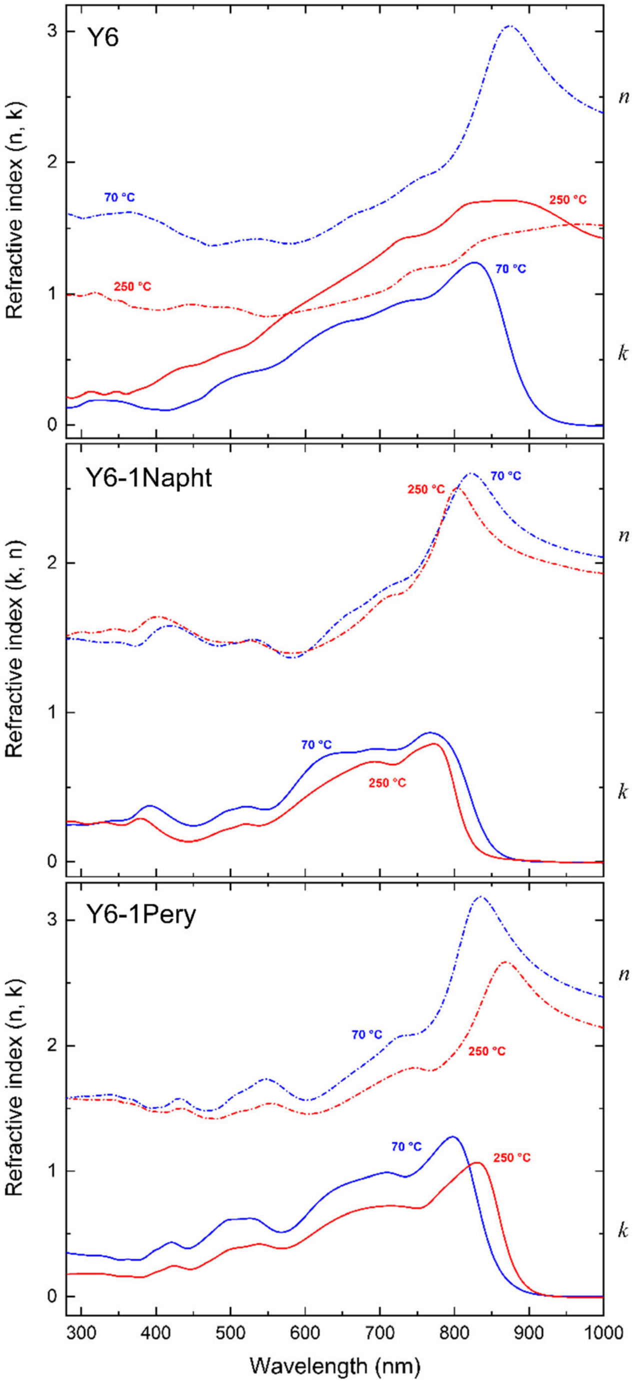

Figure 8. Plots of the refractive index (*k*, *n*) of **Y6** and **Y6 derivatives** thin-film samples. The samples were annealed first at 70 °C (blue) and then at 250 °C (red).

VASE was collected for the gradually annealed samples at the location of two annealing temperatures, namely 70 °C (blue traces) and 250 °C (red lines). From this set of measurements, hypochromic shifts on increasing annealing temperature could be thus detected for **Y6** and **Y6-1Napht**, while for **Y6-1Pery**, a bathochromic shift can be highlighted. This is in agreement with the results drawn from PL investigations. The refractive index and the integrated extinction coefficient seem to decrease upon annealing at 250 °C. As the density of dipoles is expected to increase upon crystallization, the observed decrease can be related to 1) change in orientation toward a more isotropic film; 2) dewetting or an increase in porosity; or 3) smaller dipole of the different polymers following the selection rules (valid for H-aggregation only).

In the past set of experiments, we investigated the potential application of the synthesized **Y6-based** derivatives in OSCs in combination with the donor **PM6**. We employed a combinatorial screening methodology to investigate the optimal active layer thickness of these blends in an inverted device structure (see Supporting Information for experimental details).[46] The OPV parameters for each material at room temperature are reported and compared in **Table 3**, and the photovoltaic parameters as a function of active layer thickness are shown in Figure S39–S41, Supporting Information. The optimized blade-coated **Y6:PM6** solar cell leads to an efficiency of 8.4%, while **Y6-1Napht** and **Y6-1Pery** solar cells have efficiencies between 4% and 4.5%, respectively. The lower performance of Y6 derivates primarily arises not only from an inferior short-circuit current (J_{SC}) but also due to a lower fill factor (FF). This inferior J_{SC} observed cannot be attributed to absorption losses, as evidenced by the comparable absorption profiles of both **Y6-1Napht** and **Y6-1Pery** to that of the **Y6** (Figure 3a) and a similar maximum extinction coefficient displayed in Figure 8. In contrast, the pronounced rigidity and planarity of the backbones in **Y6-1Napht** and **Y6-1Pery** may be leading to an unfavorable microstructure that limits charge generation or collection, as it was confirmed by theoretical calculations of different dimeric structures with similar energy values (Figure 5). On the other hand, the V_{oc} is larger with respect to the **Y6** reference, as expected from the energy levels deduced using CV and, possibly, their lower reorganization energies (see above).

As we have shown earlier, the microstructure of these acceptors can be varied by applying thermal annealing. Therefore, to evaluate if an enhanced order could improve the electronic properties of the blends, and thus the photocurrent, we have investigated the effect of annealing the devices. We explored a thermal treatment by annealing of the active layer based on **Y6-1Napht** and **Y6-1Pery** with **PM6** at various temperatures (80, 100, and 150 °C). The best efficiencies as a function of the annealing temperatures for the three different systems are shown in **Figure 9**a. The OPV parameters of each blend versus the annealing temperature are shown in Table 3, as derived from the *J–V* curve for each device (Figure 9b). **Y6:PM6** blend showed an increased

Table 3. Comparison of the OPV parameters for the best pixel of each Y6 derivative at room temperature and in the best annealing conditions.

Parameter	Y6:PM6		Y6-1Napht:PM6		Y6-1Pery:PM6	
	RT	ann.	RT	ann.	RT	ann.
Efficiency [%]	8.4	10.0	4.0	5.5	4.4	5.5
J_{sc} [mA cm^{-2}]	−20.2	−21.2	−13.0	−13.3	−13.0	−15.9
V_{oc} [V]	0.76	0.77	0.75	0.87	0.84	0.85
FF [%]	56.8	60.7	41.7	47.0	40.3	41.6

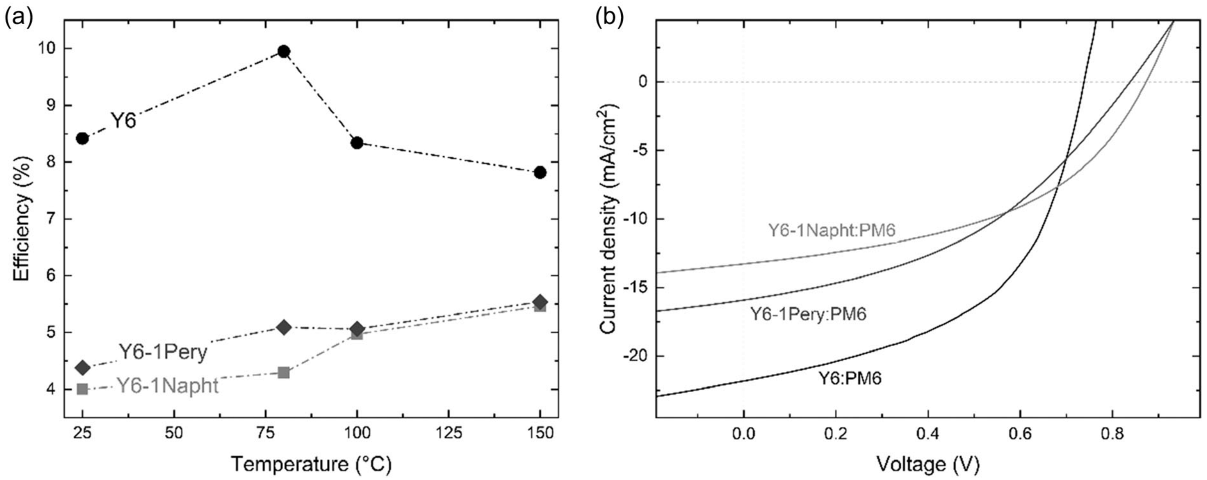

Figure 9. a) Plot of the efficiencies of the organic solar cells based on **Y6**, **Y6-1Napht,** and **Y6-1Pery** with **PM6** as a function of the annealing temperature of the solar cell. b) *J–V* curves of optimized solar cells.

performance of 1.5% in efficiency with an annealing temperature of 80 °C, but at higher annealing temperatures, the efficiency decreases. In contrast, the efficiency of solar cells based on **Y6-1Napht:PM6** and **Y6-1Pery:PM6** blends steadily increases up to 150 °C by 1.5% and 1.2%, respectively. This effect could be attributed to the lower organization energy of **Y6-1Napht** and **Y6-1Pery** with respect to **Y6** and/or the molecule's larger size, which may slow down diffusion as it has been observed in dimers. Despite the increase in performance with the thermal treatment, the performance of **Y6-1Napht:PM6** and **Y6-1Pery: PM6** solar cells is still lower than that of **Y6:PM6** due to a significantly lower J_{SC}, while the V_{oc} of **Y6-1Napht:PM6** and **Y6-1Pery:PM6** is around 0.1 V higher than that of **Y6:PM6**, as expected due to its higher-lying LUMO levels compared to the LUMO of **Y6**. Thus, our approach to extended acceptor core in A–DA′D–A FREAs leads to a similar photovoltaic result than previous study reports,[47] where the V_{oc} is increased and limited J_{SC}.

3. Conclusions

The introduction of electron-deficient rylenimide units is an effective strategy to modulate the optical and morphological properties of π-conjugated scaffolds. This study herein provides a versatile synthetic approach to design core-modified Y6-based organic semiconductors with fused electroactive aryleneimides. This chemical modification paves the way to obtain A–DA'–D–A quinoxaline-based assemblies with extended 2D conjugation, featuring fluorinated end-capped electron-acceptor units, named **Y6-1Napht** and **Y6-1Pery**. All the new π-extended assemblies have been fully characterized, and their optical and electrochemical characteristics confirm that the core-engineering strategy allows a fine tuning of the properties, which also shows a strong dependence on the length of the rylene unit. Regarding the energy levels of the frontier molecular orbitals, it is worth noting that while **Y6-1Napht** presents a similar HOMO energy level in comparison with that of Y6, the incorporation of the perylene derivative with a higher π-extended system leads to a higher destabilization of the HOMO energy level in **Y6-1Pery**. This experimental evidence is also consistent with the data obtained by DFT quantum chemical calculation experiments at the B3LYP/6-31G** theoretical level.

To study their microstructure in thin films, we measured the temperature-dependent PL with temperatures between 70 and 250 °C. These measurements show 1) the importance of the type of substitution on the shifts of the emission maximum, which clearly affects the energy level of the π-extended arrays, 2) a good agreement with the theoretical dimeric scenario proposed, which highlights the importance of the π-extended surface of the molecule in tuning the type of π–π interactions in the molecules, and 3) a good correlation with the evidence obtained by VASE, where hypochromic and bathochromic shifts in the refractive indexes of the **Y6**, **Y6-1Napht,** and **Y6-1Pery** semiconductors are detected upon annealing.

Finally, preliminary results in OSCs are also reported, which gives us insight into the design and synthesis of core-modified FREAs. The combination of these rylenimide electron-acceptor systems with the **PM6** donor was screened using a high-throughput methodology to obtain the optimal conditions for these electroactive blends. The results obtained from the measurements show a strong dependence of these materials on an annealing treatment, improving their performances by 1.2% and 1.5% for **Y6-1Napht** and **Y6-1Pery**, respectively, to reach maximum efficiency values of 5.5%.

Thus, in summary, the core engineering strategy presented herein shows its effectiveness in terms of optimization of frontier molecular orbitals energy levels, absorption wavelength, and reorganization energies, which strongly depend on the length of the central core, to provide novel NFAs for OPV.

Supporting Information

Supporting Information is available from the Wiley Online Library or from the author.

Acknowledgements

This work was financially supported by the Spanish Ministry of Science and Innovation (grant nos. PID2022-138908NB-C33, PID2021-128924OB-I00, PID2020-113142RB-C21, PLEC2021-007906, TED2021-131911B-I00, TED2021-129886B-C43, and TED2021-129416A-I00) and the Complutense University of Madrid (INV.GR.00.1819.10759). F.S.B. and M.J.A.N. gratefully acknowledge Universidad Rey Juan Carlos for their predoctoral and postdoctoral contracts. L.P. acknowledges funding by the "Toso Montanari" scholarship N.3280 (ID 1887). S.R.G. is thankful to Marie Sklodowska-Curie Actions (H2020-MSCA-IF-2020) for Grant Agreement No. 101025608, IDEAL. J.I.M. also acknowledges funding from Comunidad de Madrid (grant nos. S2018/NMT-4367 and Y2020/NMT-6469).

Conflict of Interest

The authors declare no conflict of interest.

Data Availability Statement

The data that support the findings of this study are available from the corresponding author upon reasonable request.

Keywords

annealing, frontier molecular orbitals, organic solar cells, photoluminescence, quantum calculations, rylenimide, Y6

Received: February 1, 2024
Published online: February 22, 2024

---

[1] Y. Lin, J. Wang, Z.-G. Zhang, H. Bai, Y. Li, D. Zhu, X. Zhan, *Adv. Mater.* **2015**, *27*, 1170.

[2] a) S.-L. Chang, F.-Y. Cao, W.-C. Huang, P.-K. Huang, K.-H. Huang, C.-S. Hsu, Y.-J. Cheng, *ACS Energy Lett.* **2018**, *3*, 1722; b) Z. Zhang, J. Miao, Z. Ding, B. Kan, B. Lin, X. Wan, W. Ma, Y. Chen, X. Long, C. Dou, J. Zhang, J. Liu, L. Wang, *Nat. Commun.* **2019**, *10*, 3271; c) H. Feng, X. Song, Z. Zhang, R. Geng, J. Yu, L. Yang, D. Baran, W. Tang, *Adv. Funct. Mater.* **2019**, *29*, 1903269.

[3] W. Zhao, S. Li, H. Yao, S. Zhang, Y. Zhang, B. Yang, J. Hou, *J. Am. Chem. Soc.* **2017**, *139*, 7148.

[4] a) Y. Tong, Z. Xiao, X. Du, C. Zuo, Y. Li, M. Lv, Y. Yuan, C. Yi, F. Hao, Y. Hua, T. Lei, Q. Lin, K. Sun, D. Zhao, C. Duan, X. Shao, W. Li, H.-L. Yip, Z. Xiao, B. Zhang, Q. Bian, Y. Cheng, S. Liu, M. Cheng, Z. Jin, S. Yang, L. Ding, *Sci. Chin. Chem.* **2020**, *63*, 758; b) Q. Wei, J. Yuan, Y. Yi, *Nat. Sci. Rev.* **2021**, *8*, nwab121; c) J. Yuan, Y. Zhang, L. Zhou, G. Zhang, H.-L. Yip, T.-K. Lau, X. Lu, C. Zhu, H. Peng, P. A. Johnson, M. Leclerc, Y. Cao, J. Ulanski, Y. Li, Y. Zou, *Joule* **2019**, *3*, 1140; d) Q. Liu, Y. Jiang, K. Jin, J. Qin, J. Xu, W. Li, J. Xiong, J. Liu, Z. Xiao, K. Sun, S. Yang, X. Zhang, L. Ding, *Sci. Bull.* **2020**, *65*, 272; e) K. Jin, Z. Xiao, L. Ding, *J. Semicond.* **2021**, *42*, 060502.

[5] T. J. Aldrich, M. Matta, W. Zhu, S. M. Swick, C. L. Stern, G. C. Schatz, A. Facchetti, F. S. Melkonyan, T. J. Marks, *J. Am. Chem. Soc.* **2019**, *141*, 3274.

[6] a) S. Liu, J. Yuan, W. Deng, M. Luo, Y. Xie, Q. Liang, Y. Zou, Z. He, H. Wu, Y. Cao, *Nat. Photonics* **2020**, *14*, 300; b) K. Jiang, Q. Wei, J. Y. L. Lai, Z. Peng, H. K. Kim, J. Yuan, L. Ye, H. Ade, Y. Zou, H. Yan, *Joule* **2019**, *3*, 3020.

[7] a) B. Kan, H. Feng, X. Wan, F. Liu, X. Ke, Y. Wang, Y. Wang, H. Zhang, C. Li, J. Hou, Y. Chen, *J. Am. Chem. Soc.* **2017**, *139*, 4929; b) Y. Liu, Z. Zhang, S. Feng, M. Li, L. Wu, R. Hou, X. Xu, X. Chen, Z. Bo, *J. Am. Chem. Soc.* **2017**, *139*, 3356; c) W. Li, Z. Xiao, J. Cai, J. A. Smith, E. L. K. Spooner, R. C. Kilbride, O. S. Game, X. Meng, D. Li, H. Zhang, M. Chen, R. S. Gurney, D. Liu, R. A. L. Jones, D. G. Lidzey, L. Ding, T. Wang, *Nano Energy* **2019**, *61*, 318; d) Q. Wang, M. Li, X. Zhang, Y. Qin, J. Wang, J. Zhang, J. Hou, R. A. J. Janssen, Y. Geng, *Macromolecules* **2019**, *52*, 4464; e) J. Yuan, Y. Zhang, L. Zhou, C. Zhang, T.-K. Lau, G. Zhang, X. Lu, H.-L. Yip, S. K. So, S. Beaupré, M. Mainville, P. A. Johnson, M. Leclerc, H. Chen, H. Peng, Y. Li, Y. Zou, *Adv. Mater.* **2019**, *31*, 1807577; f) Z. Zhou, W. Liu, G. Zhou, M. Zhang, D. Qian, J. Zhang, S. Chen, S. Xu, C. Yang, F. Gao, H. Zhu, F. Liu, X. Zhu, *Adv. Mater.* **2020**, *32*, 1906324.

[8] S. H. Park, A. Roy, S. Beaupré, S. Cho, N. Coates, J. S. Moon, D. Moses, M. Leclerc, K. Lee, A. J. Heeger, *Nat. Photonics* **2009**, *3*, 297.

[9] P. Cong, Z. Wang, Y. Geng, Y. Meng, C. Meng, L. Chen, A. Tang, E. Zhou, *Nano Energy* **2023**, *105*, 108017.

[10] D. Gedefaw, M. Prosa, M. Bolognesi, M. Seri, M. R. Andersson, *Adv. Energy Mater.* **2017**, *7*, 1700575.

[11] H. Lai, H. Chen, Y. Zhu, H. Wang, Y. Li, F. He, *Macromolecules* **2022**, *55*, 3353.

[12] a) T. Hasegawa, M. Ashizawa, K. Aoyagi, H. Masunaga, T. Hikima, H. Matsumoto, *Org. Lett.* **2017**, *19*, 3275; b) T. Hasegawa, M. Ashizawa, J. Hiyoshi, S. Kawauchi, J. Mei, Z. Bao, H. Matsumoto, *Polym. Chem.* **2016**, *7*, 1181.

[13] C. Zhu, K. An, W. Zhong, Z. Li, Y. Qian, X. Su, L. Ying, *Chem. Commun.* **2020**, *56*, 4700.

[14] a) X. Ge, D. Chen, Y. Yin, Z. Zheng, F. Guo, S. Gao, Y. Zhang, *Synth. Met.* **2022**, *286*, 117054; b) M. R. Biradar, S. V. Bhosale, P. P. Morajakar, S. V. Bhosale, *Fuel* **2022**, *310*, 122487; c) J. Wang, X. Zhan, *Trends Chem.* **2019**, *1*, 869; d) P. Cheng, X. Zhao, X. Zhan, *Acc. Mater. Res.* **2022**, *3*, 309.

[15] Y. Xie, T. Fujimoto, S. Dalgleish, Y. Shuku, M. M. Matsushita, K. Awaga, *J. Mater. Chem. C* **2013**, *1*, 3467.

[16] Y. Zhang, F. Cai, J. Yuan, Q. Wei, L. Zhou, B. Qiu, Y. Hu, Y. Li, H. Peng, Y. Zou, *Phys. Chem. Chem. Phys.* **2019**, *21*, 26557.

[17] R. P. Ortiz, H. Herrera, M. J. Mancheño, C. Seoane, J. L. Segura, P. M. Burrezo, J. Casado, J. T. L. Navarrete, A. Facchetti, T. J. Marks, *Chem.: A Eur. J.* **2013**, *19*, 12458.

[18] P. de Echegaray, M. J. Mancheño, I. Arrechea-Marcos, R. Juárez, G. López-Espejo, J. T. López Navarrete, M. M. Ramos, C. Seoane, R. P. Ortiz, J. L. Segura, *J. Org. Chem.* **2016**, *81*, 11256.

[19] T. F. Otero, J. Arias-Pardilla, H. Herrera, J. L. Segura, C. Seoane, *Phys. Chem. Chem. Phys.* **2011**, *13*, 16513.

[20] a) M. J. Alonso-Navarro, A. Harbuzaru, M. Martínez-Fernández, P. Pérez Camero, J. T. López Navarrete, M. M. Ramos, R. Ponce Ortiz, J. L. Segura, *J. Mater. Chem. C* **2021**, *9*, 7936; b) R. P. Ortiz, H. Herrera, R. Blanco, H. Huang, A. Facchetti, T. J. Marks, Y. Zheng, J. L. Segura, *J. Am. Chem. Soc.* **2010**, *132*, 8440.

[21] H. Herrera, P. de Echegaray, M. Urdanpilleta, M. J. Mancheño, E. Mena-Osteritz, P. Bäuerle, J. L. Segura, *Chem. Commun.* **2013**, *49*, 713.

[22] R. Adel, E. Gala, M. J. Alonso-Navarro, E. Gutierrez-Fernandez, J. Martín, M. Stella, E. Martinez-Ferrero, A. de la Peña, A. Harbuzaru, M. M. Ramos, R. P. Ortiz, J. L. Segura, M. Campoy-Quiles, *J. Mater. Chem. C* **2022**, *10*, 1698.

[23] I. Arrechea-Marcos, P. de Echegaray, M. J. Mancheño, M. C. Ruiz Delgado, M. M. Ramos, J. A. Quintana, J. M. Villalvilla, M. A. Díaz-García, J. T. López Navarrete, R. Ponce Ortiz, J. L. Segura, *Phys. Chem. Chem. Phys.* **2017**, *19*, 6206.

[24] M. J. Alonso-Navarro, E. Gala, M. M. Ramos, R. Ponce Ortiz, J. L. Segura, *Electron. Mater.* **2021**, *2*, 222.
[25] M. J. Alonso-Navarro, A. Harbuzaru, P. de Echegaray, I. Arrechea-Marcos, A. Harillo-Baños, A. de la Peña, M. M. Ramos, J. T. López Navarrete, M. Campoy-Quiles, R. Ponce Ortiz, J. L. Segura, *J. Mater. Chem. C* **2020**, *8*, 15277.
[26] M. J. Alonso-Navarro, J. Barrio, S. Royuela, N. Karjule, M. M. Ramos, J. I. Martínez, M. Shalom, J. L. Segura, *RSC Adv.* **2021**, *11*, 2701.
[27] F. Suárez-Blas, J. Li, M. J. Alonso-Navarro, A. Harbuzaru, R. Ponce Ortiz, M. M. Ramos, M. Shalom, J. Barrio, J. L. Segura, *Adv. Sustainable Syst.* **2023**, *7*, 2200339.
[28] D. Michalska, R. Wysokiński, *Chem. Phys. Lett.* **2005**, *403*, 211.
[29] A. S. Davydov, *Soviet Phys. Usp.* **1964**, *7*, 145.
[30] F. Liu, L. Zhou, W. Liu, Z. Zhou, Q. Yue, W. Zheng, R. Sun, W. Liu, S. Xu, H. Fan, L. Feng, Y. Yi, W. Zhang, X. Zhu, *Adv. Mater.* **2021**, *33*, 2100830.
[31] Y. Shi, Y. Chang, K. Lu, Z. Chen, J. Zhang, Y. Yan, D. Qiu, Y. Liu, M. A. Adil, W. Ma, X. Hao, L. Zhu, Z. Wei, *Nat. Commun.* **2022**, *13*, 3256.
[32] H. B. Frisch, G. E. Robb, M. A. Cheeseman, J. R. Scalmani, G. Barone, V. Petersson, G. A. Nakatsuji, H. Li, X. Caricato, M. Marenich, A. V. Bloino, J. Janesko, B. G. Gomperts, R. Mennucci, B. Hratchian, H. P. Ortiz, J. V. Izmaylov, A. F. Sonnenberg, J. L. Williams-Young, D. Ding, F. Lipparini, F. Egidi, F. Goings, J. Peng, B. Petrone, A. Henderson, T. Ranasinghe, D. Zakrzewski, V. G. Gao, J. Rega, et al., *Gaussian 16, Revision C.01*, Gaussian, Inc., Wallingford, CT **2016**.
[33] a) L. A. Curtiss, M. P. McGrath, J. P. Blaudeau, N. E. Davis, R. C. Binning, L. Radom, *J. Chem. Phys.* **1995**, *103*, 6104; b) A. D. Becke, *J. Chem. Phys.* **1993**, *98*, 5648.
[34] W. Zhu, A. P. Spencer, S. Mukherjee, J. M. Alzola, V. K. Sangwan, S. H. Amsterdam, S. M. Swick, L. O. Jones, M. C. Heiber, A. A. Herzing, G. Li, C. L. Stern, D. M. DeLongchamp, K. L. Kohlstedt, M. C. Hersam, G. C. Schatz, M. R. Wasielewski, L. X. Chen, A. Facchetti, T. J. Marks, *J. Am. Chem. Soc.* **2020**, *142*, 14532.
[35] R. Liao, X. Ma, C. Tang, Y. Liu, W. Zheng, Y. Ma, Q. Tu, W. Lin, Y. Yi, Q. Zheng, *J. Mater. Chem. A* **2022**, *10*, 23915.
[36] L. Ueberricke, I. Ciubotaru, F. Ghalami, F. Mildner, F. Rominger, M. Elstner, M. Mastalerz, *Chem.: A Eur. J.* **2020**, *26*, 11634.
[37] S. Pluczyk-Malek, D. Honisz, A. Akkuratov, P. Troshin, M. Lapkowski, *Electrochim. Acta* **2021**, *368*, 137540.
[38] a) M. Erray, M. Hanine, E.-M. Boufounas, A. El Amrani, *Eur. Phys. J. Appl. Phys.* **2018**, *82*, 30201; b) J. Zhang, W. Liu, M. Zhang, Y. Liu, G. Zhou, S. Xu, F. Zhang, H. Zhu, F. Liu, X. Zhu, *iScience* **2019**, *19*, 883.
[39] J. Zhang, W. Liu, G. Zhou, Y. Yi, S. Xu, F. Liu, H. Zhu, X. Zhu, *Adv. Energy Mater.* **2020**, *10*, 1903298.
[40] M. Campoy-Quiles, M. Sims, P. G. Etchegoin, D. D. C. Bradley, *Macromolecules* **2006**, *39*, 7673.
[41] L. Ciammaruchi, O. Zapata-Arteaga, E. Gutiérrez-Fernández, J. Martin, M. Campoy-Quiles, *Mater. Adv.* **2020**, *1*, 2846.
[42] L. Zhu, J. Zhang, Y. Guo, C. Yang, Y. Yi, Z. Wei, *Angew. Chem. Int. Ed.* **2021**, *60*, 15348.
[43] S. Ma, Y. Liu, J. Zhang, B. Xu, W. Tian, *J. Phys. Chem. Lett.* **2020**, *11*, 10504.
[44] E. Gutierrez-Fernandez, A. D. Scaccabarozzi, A. Basu, E. Solano, T. D. Anthopoulos, J. Martín, *Adv. Sci.* **2022**, *9*, 2104977.
[45] J. Yan, X. Rodríguez-Martínez, D. Pearce, H. Douglas, D. Bili, M. Azzouzi, F. Eisner, A. Virbule, E. Rezasoltani, V. Belova, B. Dörling, S. Few, A. A. Szumska, X. Hou, G. Zhang, H.-L. Yip, M. Campoy-Quiles, J. Nelson, *Energy Environ. Sci.* **2022**, *15*, 2958.
[46] E. Pascual-San-José, X. Rodríguez-Martínez, R. Adel-Abdelaleim, M. Stella, E. Martínez-Ferrero, M. Campoy-Quiles, *J. Mater. Chem. A* **2019**, *7*, 20369.
[47] K. C. Song, B. J. Kim, W. Sung, S. G. Han, S. Chung, J. Lee, K. Cho, *J. Mater. Chem. C* **2023**, *11*, 5354.